



PAPER • OPEN ACCESS

# Targeted micro-heterogeneity in bioinks allows for 3D printing of complex constructs with improved resolution and cell viability

To cite this article: Bruna R Maciel *et al* 2023 *Biofabrication* **15** 045013

View the [article online](#) for updates and enhancements.

## You may also like

- [A biofabrication method to align cells within bioprinted photocrosslinkable and cell-degradable hydrogel constructs via embedded fibers](#)  
Margaret E Prendergast, Matthew D Davidson and Jason A Burdick
- [Assessment methodologies for extrusion-based bioink printability](#)  
Gregory Gillispie, Peter Prim, Joshua Copus *et al.*
- [Egg white improves the biological properties of an alginate-methylcellulose bioink for 3D bioprinting of volumetric bone constructs](#)  
Suihong Liu, David Kilian, Tilman Ahlfeld *et al.*

# Biofabrication



## PAPER

### OPEN ACCESS

RECEIVED  
24 April 2023

REVISED  
29 July 2023

ACCEPTED FOR PUBLICATION  
8 August 2023

PUBLISHED  
21 August 2023

Original content from this work may be used under the terms of the [Creative Commons Attribution 4.0 licence](https://creativecommons.org/licenses/by/4.0/).

Any further distribution of this work must maintain attribution to the author(s) and the title of the work, journal citation and DOI.



## Targeted micro-heterogeneity in bioinks allows for 3D printing of complex constructs with improved resolution and cell viability

Bruna R Maciel<sup>1,\*</sup> , Alisa Grimm<sup>2</sup>, Claude Oelschlaeger<sup>1</sup>, Ute Schepers<sup>2</sup> and Norbert Willenbacher<sup>1</sup>

<sup>1</sup> Institute of Mechanical Process Engineering and Mechanics, Karlsruhe Institute of Technology (KIT), Karlsruhe, Germany

<sup>2</sup> Institute of Functional Interfaces, Karlsruhe Institute of Technology (KIT), Karlsruhe, Germany

\* Author to whom any correspondence should be addressed.

E-mail: [bruna.maciel@kit.edu](mailto:bruna.maciel@kit.edu)

**Keywords:** bioprinting, hydrogels, micro-heterogeneity, bioinks, wall slip

Supplementary material for this article is available [online](#)

### Abstract

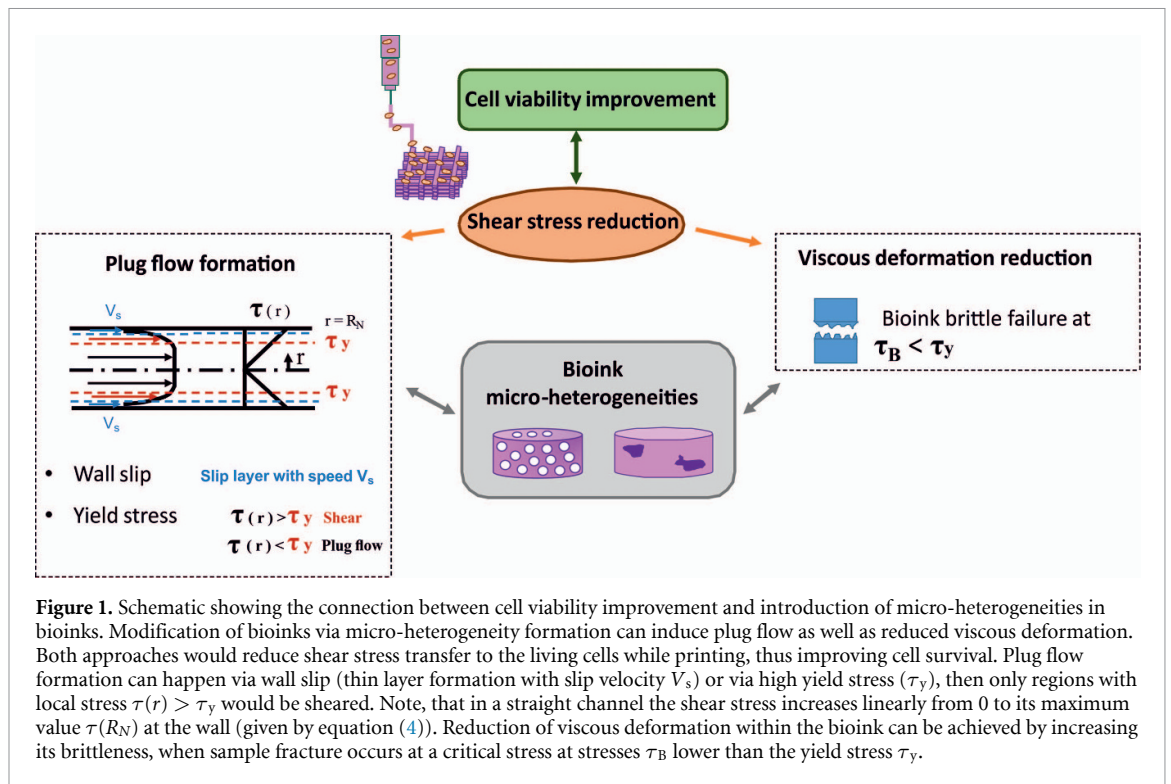
Three-dimensional bioprinting is an evolving versatile technique for biomedical applications. Ideal bioinks have complex micro-environment that mimic human tissue, allow for good printing quality and provide high cell viability after printing. Here we present two strategies for enhancing gelatin-based bioinks heterogeneity on a 1–100  $\mu\text{m}$  length scale resulting in superior printing quality and high cell viability. A thorough spatial and micro-mechanical characterization of swollen hydrogel heterogeneity was done using multiple particle tracking microrheology. When poly(vinyl alcohol) is added to homogeneous gelatin gels, viscous inclusions are formed due to micro-phase separation. This phenomenon leads to pronounced slip and superior printing quality of complex 3D constructs as well as high human hepatocellular carcinoma (HepG2) and normal human dermal fibroblast (NHDF) cell viability due to reduced shear damage during extrusion. Similar printability and cell viability results are obtained with gelatin/nanoclay composites. The formation of polymer/nanoclay clusters reduces the critical stress of gel fracture, which facilitates extrusion, thus enhancing printing quality and cell viability. Targeted introduction of micro-heterogeneities in bioinks through micro-phase separation is an effective technique for high resolution 3D printing of complex constructs with high cell viability. The size of the heterogeneities, however, has to be substantially smaller than the desired feature size in order to achieve good printing quality.

## 1. Introduction

Three-dimensional bioprinting offers a vast array of possibilities for biomedical applications. In this versatile biofabrication process, living cells can be deposited in specific positions in a 3D construct with desired geometry. In comparison to other methods, extrusion based bioprinting (EBB) is the most used technique due to low cost, ease of use and a broader range of hydrogel materials available to be used as bioink [1]. Hydrogels for tissue engineering applications often consist of mixtures of biopolymers such as gelatin, alginate, chitosan or gellan gum with synthetic polymers, poly(vinyl alcohol) (PVA), polyacrylate hydrogels or poly(ethylene glycol) for instance, in order to improve mechanical properties or biocompatibility [2–4]. More specifically, mixtures of gelatin with PVA have been described as promising

composites for cell culture scaffolds [5, 6] and tissue regeneration [7]. Many of these composite materials and hydrogels have been valued for their low stiffness and large pore size, which is a key requisite for tissue engineering. However, many other applications such as hydrogel drug delivery or bone reconstruction require much more constrained mechanical properties. A method to enhance these properties is nanoparticle reinforcement [8, 9]. Nanosilicate composites, such as mixtures of biopolymers with Laponite® clay nanoparticles, have been widely investigated for tissue engineering constructs due to its biocompatibility and degradation in nontoxic products [10–13].

One crucial requirement for EBB is finding bioink materials that allow for high printing quality, i.e. high resolution and good mechanical stability of the printed construct while providing high biocompatibility and cell viability despite significant shear stresses



that may be present during bioprinting [14, 15]. 3D printing of complex structures has been described using the FRESH technology with collagen bio-inks and support materials that can be melted away [16] or using the NICE technique to print GelMA, kappa-carrageenan and nanosilicates by increasing the printing temperature to 37 °C [17]. However, there is a lack of bioink materials that allow room temperature printing of self-standing structures with high cell viability.

Another important aspect in the search for bioink materials is the need of more complex and heterogeneous engineered hydrogel composites in order to mimic the native human tissue microenvironment [15, 18–20]. Moreover, a lack of control over micro-heterogeneity formation in hydrogels and shortage of adequate methods for characterizing microstructural heterogeneity in the hydrated state is also a challenge to be overcome. Limitations on the use of currently available imaging methods for hydrogel microstructure characterization have been reported in the literature [21–23]. Commonly used methods for imaging hydrogels include scanning electron microscopy (SEM), which gives morphological information of dried samples surfaces, and x-ray micro-tomography ( $\mu$ CT), which is able to image the three-dimensional structure of the sample. However, sample processing such as drying and coating with conductive material which is normally required for SEM, or the need of a contrast agent as in  $\mu$ CT, leads to difficulties in resolution, limited depth penetration, artifact

production or even destruction of the original 3D hydrogel microstructure, generating inaccurate results. Multiple particle tracking (MPT) technique, a micro-rheology method, is an effective tool for microstructural visualization and local flow behavior characterization without sample modification, especially in cases where other microscopy methods fail. This technique has been employed for viscoelastic and microstructural characterization of hydrated food emulsions and gels [24]. To our knowledge so far, there are a few published data on visualization of biocompatible hydrogels micro-heterogeneities using MPT [25–28].

Introduction of micro-heterogeneities has the potential to confer biomechanical as well as biochemical gradients to the bioink, resulting in complex materials that better resemble human tissue physiological conditions [29]. There is an unambiguous relationship between shear forces and cell damage during extrusion-based printing [30, 31]. Strategies for protecting living cells from shear deformation and stresses during the extrusion process and consequently improving cell survival involve formation of a plug-like flow [32] or reduced viscous deformation of the bioink (figure 1). Both strategies confer the bioink a lower capacity of transferring shear stress to the living cells. Plug flow is expected when wall slip takes place as well as when bioink yield stress, i.e. the stress necessary for a material to start flowing, is very high. The ability of a bioink to exhibit plastic deformation can be reduced by increasing its brittleness.

Particularly, little viscous deformation occurs when brittle failure sets in at stresses lower than the yield stress. In this study, the conducted approach for limiting shear force transfer between the carrying material and the living cells include the targeted introduction of micro-heterogeneities in the bioink (figure 1).

In order to modify the hydrogel mechanical properties and hence decrease shear force transfer during extrusion, two strategies for inducing micro-heterogeneity formation in gelatin based bioinks for EBB are presented in this work. The first strategy is the addition of a polymer solution (PVA) to a homogeneous gelatin hydrogel and the second is the incorporation of clay nanoparticles (Laponite) into gelatin gels. The MPT technique was employed to get new insight into the microstructural and micromechanical properties of hydrogels in the hydrated state. Heterogeneity formation via different mechanisms of micro-phase separation on the length scale 1–100  $\mu\text{m}$  was characterized and its impact on the bulk elasticity, printability and cell viability was carefully analyzed. Hydrogel bulk mechanical properties were characterized employing classical rotational as well as capillary rheometry and uniaxial compression tests. Rotational rheometry allowed for wall slip as well as brittle failure visualization and the determination of gel elasticity, slip velocity as well as slip and fracture stresses. Wall slip behavior also shows up in apparent viscosity data obtained from capillary rheometry, while Young's modulus was obtained with uniaxial compression tests. Finally, moderately heterogeneous hydrogels allowed 3D printing of self-standing complex constructs at room temperature without a support bath and provided high cell viability after 7 d of cell culture.

## 2. Experimental section

### 2.1. Hydrogel preparation

Gelatin extra pure (gold, 180 Bloom) was purchased from Carl Roth (Karlsruhe, Germany). PVA (Mowiol® 4-98,  $M_w \sim 27\,000\text{ g mol}^{-1}$ ) was purchased from Sigma- Aldrich Chemie GmbH (Taufkirchen, Germany). Dulbecco's Modified Eagle's Medium (DMEM w: 4.5  $\text{g l}^{-1}$  glucose, w: L-glutamine, w: sodium pyruvate, w/o: phenol red, w: 3.7  $\text{g l}^{-1}$   $\text{NaHCO}_3$ ) was purchased from PAN Biotech (Aidenbach, Germany). Laponite-XLG XR was purchased from BYK-Chemie GmbH (Wesel, Germany). Gelatin and PVA solutions were obtained stirring the powder with DMEM at 40 °C and ultrapure water at 90 °C, respectively, at approximately 100 rpm for 10 min. Polymer solutions were sterilized using polyethersulfone membrane filters (pore size 0.22  $\mu\text{m}$ ). Two-polymer hydrogels were prepared by mixing the PVA solution with the gelatin solution at desired concentrations with the ratio gelatin

**Table 1.** Detailed composition of the gelatin-based hydrogels.

Hydrogel	Gelatin	PVA	Laponite
6G	6%	—	—
6G2P	6%	2%	—
6G4P	6%	4%	—
6G0.2L	6%	—	0.2%
6G0.4L	6%	—	0.4%
8G2P	8%	2%	—
8G4P	8%	4%	—

solution:PVA solution 8:2 for 10 min at 100 rpm. For example, 10 ml of the sample 6G2P (6% gelatin + 2% PVA, table 1) would be prepared by mixing 8 ml of 7.5% gelatin in DMEM solution with 2 ml of 10%PVA aqueous solution. Hydrogels containing nanoparticle were produced the following way: Laponite XLG nanoparticles were dispersed in ultrapure water with a planetary mixer (Speedmixer, Hauschild GmbH & Co KG, Hamm, Germany) for 10 min at 2500 rpm. Laponite composites were prepared by mixing gelatin solution with the Laponite suspension with the ratio gelatin solution:Laponite suspension 8:2 for 10 min at 2500 rpm. For example, 10 ml of the sample 6G0.2L (6% gelatin + 0.2% Laponite, table 1) would be prepared by mixing 8 ml of 7.5% gelatin in DMEM solution with 2 ml of 1% Laponite in water suspension. Gelatin/Laponite mixtures presented pH value of 8.

All measurements were conducted 24 h after sample preparation for all systems investigated here. Table 1 shows the composition details and final weight concentrations of the different ingredients for the investigated systems:

### 2.2. Macrorheology

#### 2.2.1. Rotational rheometry

A rotational rheometer (Rheoscope I, Thermo Fisher Scientific, Germany), equipped with a stainless-steel plate-plate measuring cell (diameter 20 mm, gap distance 2 mm) was used to perform small amplitude oscillatory shear experiments at 20 °C. Sandpaper (P320 grit, roughness  $R_z = 59 \pm 16\text{ mm}$ ) was attached to the parallel plates using a double-sided tape in order to avoid slip. Both tape and sandpaper were carefully cut using a round punch tool in order to obtain the exact diameter of the parallel plate geometry. The sandpaper was exchanged after each measurement in order to guarantee that it was evenly adhered to the plates.

For all gels, frequency sweeps, covering the frequency range from 0.1 to 100  $\text{rad s}^{-1}$ , were performed at a stress amplitude sufficiently small to provide a linear material response. An exemplarily amplitude sweep test showing the linear viscoelastic region (shear stress  $\tau < 220\text{ Pa}$ , for all samples) can be found in figure S1 for sample 6G4P. Frequency

sweep tests were conducted at a shear stress amplitude value of 3 Pa for all gels. The data confirmed that the storage modulus  $G'$  was essentially frequency independent and its value at frequency  $\omega = 1 \text{ rad}\cdot\text{s}^{-1}$  was determined as the bulk shear modulus  $G_0$  of the investigated gel. Shear stress ramps were applied to assess the slip behavior with smooth plate-plate fixtures (without sandpaper, diameter 25 mm). The shear stress was stepwise increased from 1 to 10 kPa and normal force values varied from 0 N to 2 N. Video recordings were performed using a high-speed camera (MikroCam II 3.1MP, Bresser, Ghede, Germany) in order to visualize the deformation of the sample rim. Slip velocity  $v_s$  at the rim of the plate was determined using equation (1), where  $n$  is the plate rotational velocity and  $r$  is the plate diameter

$$v_s = 2n\pi r. \quad (1)$$

### 2.2.2. Capillary rheometry

High shear viscosity data were determined at 20 °C using a self-assembled piston-driven capillary rheometer. The self-assembled capillary rheometer consists of a hydraulic oil pump (60 bar and  $7 \text{ l min}^{-1}$ , GKS Hydraulik, Kressbronn am Bodensee, Germany), a piston made of stainless steel with 20 mm diameter and 28.5 cm length and a self-programmed software recording piston speed as well as extrusion pressure data. The samples were forced to flow through a stainless steel capillary with 0.5 mm diameter and 80 mm length at controlled volumetric flow rates corresponding to constant shear rate values using the 20 mm diameter piston. The resulting extrusion pressure was recorded using a pressure transducer (0–50 bar, Dynisco Europe GmbH, Heilbronn, Germany).

The apparent viscosity  $\eta_s$  is given by the ratio of shear stress  $\tau$  and shear rate  $\dot{\gamma}$ :

$$\eta_s = \frac{\tau}{\dot{\gamma}} \quad (2)$$

where shear rate is given by equation (3):

$$\dot{\gamma} = \frac{4\dot{V}}{\pi R_N^3} \quad (3)$$

where  $\dot{V}$  is the volumetric flow and  $R_N$  the nozzle radius.

And the shear stress is given by equation (4):

$$\tau = \frac{\Delta p \cdot R_N}{2L} \quad (4)$$

where  $\Delta p$  is the pressure difference between the sample reservoir and the nozzle outlet measured using a pressure sensor mounted 1 cm above the nozzle inlet and  $L$  is the nozzle length.

The viscosity calculated according to equations (2)–(4) have to be treated as apparent values since these equations are only valid for Newtonian fluids. Entrance pressure loss corrections can be safely neglected, since a capillary nozzle with  $L/R_N = 160$  was used. Corrections that take into account the shear thinning behavior of the gels were not performed here.

### 2.2.3. Uniaxial compression tests

Uniaxial unconfined compression tests were performed at 20 °C using the commercial tensile testing machine Texture Analyzer TA.XTplus (Stable Micro System, UK) equipped with a 5 kg load cell. Tests were performed on cylindrically shaped gels of 5 mm height and 10 mm diameter. Samples were compressed with a plate (5 cm × 5 cm) at a compression speed of  $0.1 \text{ mm s}^{-1}$ . Young's modulus  $E$  was determined as the slope of the linear stress-strain curve in the strain region <40%.

### 2.3. Microrheology

MPT: the MPT setup used in this study is based on an inverted fluorescence widefield microscope (Axio Observer D1, Carl Zeiss) equipped with a Fluor 100x objective (numerical aperture 1.3, 100x magnification, oil immersion lens, Carl Zeiss) [33]. Green fluorescent carboxyl-functionalized polystyrene microspheres of 0.2  $\mu\text{m}$  diameter with density  $1.06 \text{ g cm}^{-3}$  and refractive index 1.59 at 589 nm were used as tracer particles (Bangs Laboratories, USA). The investigated samples including the tracer particles were placed between a microscope glass slide and a coverslip. The microscope was focused roughly halfway into the sample, i.e. at a distance of 20–40  $\mu\text{m}$  away from the surface, to minimize wall effects. 2D images (field of view  $127 \times 127 \mu\text{m}$ , frame rate  $50 \text{ frames sec}^{-1}$ ) of the fluorescent particles were recorded using a sCMOS camera Zyla X (Andor Technology). Movies of the fluctuating microspheres were analyzed using a custom MPT routine incorporated into the software Image Processing System (Visiometrics iPS) [34, 35]. Particle tracking and calculation of mean square displacement (MSD), as well as the statistical analysis of the trajectories was done using a self-written Matlab® program based on the widely used Crocker and Grier tracking algorithm [33, 36]. Tracer particles were added prior to gelation, to ensure a homogeneous distribution of the tracer particles within the sample. The local viscoelastic modulus  $G^*(\omega)$  around a sphere as a function of the frequency  $\omega$  can be determined from equation (5) [37]:

$$G^*(\omega) = \frac{k_B T}{\pi a i \omega \langle \Delta \tilde{r}^2(i\omega) \rangle} = G'(\omega) + iG''(\omega) \quad (5)$$

with  $\alpha$  being the tracer particle radius,  $k_B$  the Boltzmann constant,  $T$  the temperature and  $\langle \Delta \tilde{r}^2(i\omega) \rangle$  the MSD of the tracer particles.

Tracers trapped in an elastic network exhibit a time-independent MSD directly related to the apparent local shear modulus of this region:

$$G_{0,MPT} = \frac{2k_B T}{3\pi a \Delta r^2}. \quad (6)$$

Tracers freely diffusing in a viscous environment exhibit a linearly increasing MSD and the apparent viscosity  $\eta_{MPT}$  of the surrounding fluid is determined using equation (7) obtained from the Stokes–Einstein relation [38], and the relation  $\langle \Delta r^2(\tau) \rangle = 4D\tau$ , where  $D$  is the diffusion coefficient related to the MSD  $\langle \Delta r^2(\tau) \rangle$  as a function of the lag time  $\tau$  [39]:

$$\eta_{MPT} = \frac{k_B T}{6\pi a D}. \quad (7)$$

#### 2.4. Printing quality evaluation with extrusion based 3D printing

The gelatin-based hydrogels were printed on microscope glass slides using a pressure-controlled Voxel 8 Developer's Kit 3D printer (Voxel 8 Inc., Harvard, USA). 3 CC cartridges (Nordson EFD, Feldkirchen, Germany) and straight needles of stainless steel, (0.15 mm outlet diameter and 12 mm length, VIEWEG, Germany), were used to extrude the hydrogels in log pile pattern (self-written G-Code, 0.15 mm layer height for all cases) and in ear shape construct (Human Right Ear model by col98 available in [www.thingiverse.com/thing:1697869](http://www.thingiverse.com/thing:1697869)) with pressure values varying from 0.3 to 0.4 MPa. The print head velocity was kept at 600 mm min<sup>-1</sup> for all samples. The 3D constructs were imaged using a Digital Microscope VHX-950 F (Keyence, Neu-Isenburg, Germany) and image analysis of printing quality was performed with the software Image Processing System (Visiometrics iPS).

#### 2.5. Cell encapsulation and 3D bioprinting

Human hepatocellular carcinoma (HepG2, purchased from Sigma- Aldrich Chemie GmbH, Taufkirchen, Germany) and normal human dermal fibroblasts (NHDFs, purchased from PromoCell, Heidelberg, Germany) cells were detached from their respective cell culture flasks with trypsin-EDTA 0.25% and suspended in DMEM (high glucose). The gelatin-based gels were liquefied by heating to 37 °C. Then, 950  $\mu$ l of sample was gently mixed with 50  $\mu$ l of cell suspension (either HepG2 or NHDF) so that the bioink contained a final cell concentration of  $2.5 \times 10^6$  cells ml<sup>-1</sup>. Controls (200  $\mu$ l) were taken prior to printing and the cell-laden gelatin-based bioink was placed in a syringe and allowed to thermally gelate for 30 min–1 h

at 20 °C. The extrusion based 3D bioprinter BioSpot BP (Biofluidix GmbH, Freiburg, Germany) was used for bioprinting at 20 °C. Bioinks were 3D printed in log pile shapes with 4 layers on adhesive slides with 250  $\mu$ m straight needles of stainless steel at an extrusion rate of 0.015–0.02 mm s<sup>-1</sup> and a printing speed of 5 mm s<sup>-1</sup>. 3D printed constructs were enzymatically crosslinked with 10 wt.% (for gels evaluated on day 1) and 20 wt.% (for gels evaluated on day 7) transglutaminase (100 U g<sup>-1</sup>, kindly provided by Ajinomoto, Co., Kawasaki, Japan). The enzyme dispersion was prepared by stirring the powder with ultra-pure water at 50 °C for 10 min. The enzyme dispersion was dripped on top of the printed constructs and left for 1 h before washing with DPBS<sup>-/-</sup> (Dulbecco's phosphate buffered saline, without calcium and magnesium). 3D printed constructs were covered with 10 ml DMEM in a petri dish and furthered cultivated at 37 °C and 5%CO<sub>2</sub>. DMEM, DPBS<sup>-/-</sup> and trypsin-EDTA used in this section were purchased from Gibco® Life Technologies, Carlsbad, USA.

#### 2.6. Live/dead staining

Post printing cell viability was assessed for HepG2 cells at day 1 and NHDF cells at days 1 and 7. The supernatant cell medium was removed and the cell-laden hydrogel constructs were stained with Calcein-AM (4  $\mu$ g ml<sup>-1</sup>, Life Technologies, Carlsbad, USA) and propidium iodide (20  $\mu$ g ml<sup>-1</sup>, Sigma-Aldrich, Taufkirchen, Germany). After 30 min of incubation, the staining solution was removed, the constructs were washed twice with DPBS and then covered with cell culture medium. Z-stack images were recorded for evaluation using the confocal microscope Leica Stellaris 5 (Leica Microsystems GmbH, Wetzlar, Germany). At least three parallel images were analyzed and HepG2 cell viability was determined by the fraction of viable cells over the total cell count and NHDF cell viability was determined by the fraction of detected live cell area over the total cell area with the software ImageJ.

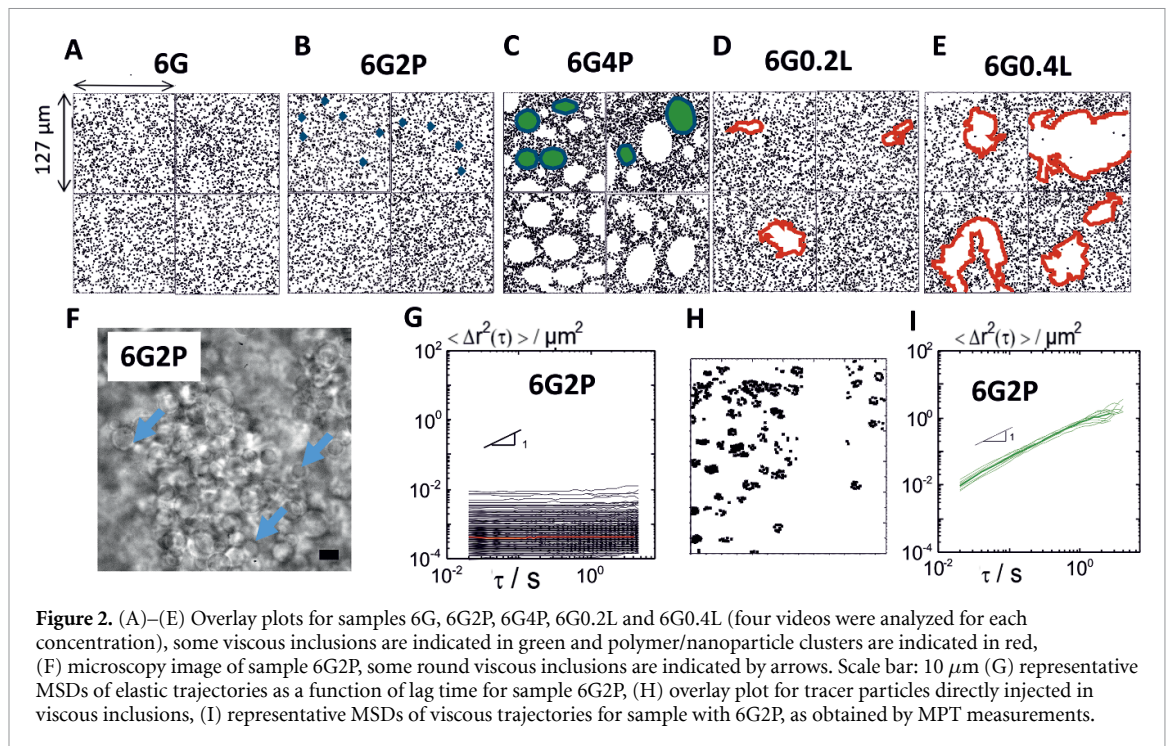
#### 2.7. Statistical analysis

Data are depicted as mean  $\pm$  SD with  $N \geq 3$  for all groups. Comparisons between different data sets were performed using one-way ANOVA with Bonferroni correction. Differences were statistically significant for  $p < 0.05$ .

### 3. Results

#### 3.1. Micro-heterogeneity characterization

We present two strategies for inducing micro-heterogeneity in gelatin hydrogels: addition of a second polymer and addition of nanoparticles. Measuring the particle distribution and particle trajectories in the bioink via MPT using fluorescent carboxyl-functionalized polystyrene microspheres



allows for the microrheology by imaging technologies. Overlay images created from 500 images taken from MPT video sequences show that pure gelatin is a homogeneous hydrogel, with tracer particles uniformly dispersed in the 6G sample (figure 2(A)). By adding a second polymer (PVA) (figures 2(B) and (C)), a heterogeneous micro-structure in the form of discrete pore-like inclusions appears, corresponding to the white areas (some are green colored) in figures 2(B) and (C)) containing no tracer particles. The round shaped inclusions can be observed in images obtained by white light microscopy (figure 2(F), sample 6G2P). The detected MSDs are time independent, indicating that all tracers are embedded in the elastic matrix environment provided by the gelatin gel for all compositions with local elasticity  $G_{0,\text{MPT}}$  in the range of 10–25 Pa (figure 2(G) shows MSD example for sample 6G2P). In order to characterize the void spaces of the gels with PVA, tracer particles were directly injected into the inclusions with a syringe (figure 2(H)). The MSDs vary linearly with time, as shown exemplarily for sample 6G2P in figure 2(I) indicating that the tracer particles are diffusing freely in the surrounding material. These inclusions are presumably formed of aqueous PVA solution. When gelatin thermal gelation occurs, PVA in solution demixes from the elastic matrix forming the beads-free, pore-like viscous inclusions while the tracer particles are arrested and remain in the gelatin elastic region. Liquid–liquid and solid–liquid separation normally depend on environmental stimuli, such as temperature or pH [40, 41]. In our study, liquid gelatin and PVA solutions were well mixed with the tracer particles at 40 °C. By

decreasing the temperature, micro-phase demixing is triggered and ceases (together with gelatin physical thermal crosslinking) when room temperature (20 °C) is reached. By increasing PVA concentration from 2 to 4 wt.%, size of the pores increases from  $5 \pm 2 \mu\text{m}$  to  $28 \pm 11 \mu\text{m}$  and local viscosity  $\eta_{\text{MPT}}$  in the pores from  $6 \pm 4 \text{ mPas}$  to  $30 \pm 4 \text{ mPas}$  (corresponding to PVA concentrations of  $\sim 5$  and  $\sim 6.5$  wt%, respectively), as obtained by MPT measurements. At the same time, the fraction of viscous area in the elastic hydrogel increases from  $2 \pm 1\%$  to  $24 \pm 5\%$ , suggesting that more PVA demixed from gelatin.

Turning to the second strategy, the addition of nanosilicate particles (Laponite-XLG XR), induces formation of densely packed micro-heterogeneities depleted of tracer beads and presumably constituted of polymer and nanoparticles aggregates (figures 2(D) and (E)). Gelatin and Laponite interact electrostatically, especially in the presence of electrolyte, such as the salts present in the aqueous solvent DMEM, leading to micro-phase separation and aggregate formation [42, 43]. By increasing Laponite concentration from 0.2 to 0.4 wt.%, agglomerate size increases from  $34 \pm 14 \mu\text{m}$  to  $82 \pm 32 \mu\text{m}$  and the fraction of micro-heterogeneities in the gel increases from  $4 \pm 3$ – $26 \pm 15\%$ , indicating that micro-phase separation was enhanced. Similar to the system with PVA, MSD of all tracers dispersed in the gelatin/Laponite matrix are time independent with  $10 \text{ Pa} < G_{0,\text{MPT}} < 25 \text{ Pa}$ . Representative MSDs of elastic trajectories as a function of lag time for sample 6G0.2L is show in figure S2.

Here we have created overlay images from video sequences obtained from MPT using fluorescent

**Table 2.** Size, viscosity and fraction of micro-heterogeneities in samples 6G2P, 6G4P, 6G0.2L and 6G0.4L.

Sample	Size/ $\mu\text{m}$	Viscosity ( $\eta_{\text{MPT}}$ )/mPas	Fraction in the gel/%
6G2P	$5 \pm 2$	$6 \pm 4$	$2 \pm 1$
6G4P	$28 \pm 11$	$30 \pm 4$	$24 \pm 5$
6G0.2L	$34 \pm 14$	—	$4 \pm 3$
6G0.4L	$82 \pm 32$	—	$26 \pm 15$

*Note,* these micro-heterogeneities characteristics are valid for the gel preparation method described here. Other preparation methods might result in micro-heterogeneities with different features.

tracers as a convenient, non-destructive means to visualize the size and shape of heterogeneities in gelatin hydrogels. In case of the viscous inclusions even the viscosity (and hence polymer concentration) of the inclusions is accessible using MPT.

Bright-field as well as fluorescence microscopy images for all hydrogels can be found in figure S3. PVA pore-like viscous inclusions in the gelatin gel can be observed via bright-field microscopy (figures 2(F) and S3). However, Laponite/gelatin aggregates can not be detected, presumably because their refractive index is very close to that of the surrounding hydrogel matrix. These micro-heterogeneities could be visualized employing fluorescence microscopy (figure S3). These results obtained for the hydrogel in hydrated state corroborate the earlier findings of Ahlfeld, Ahlfeld *et al* [11], which detected heterogeneous distribution of Laponite in dehydrated nanoclay based bioinks in terms of energy dispersive electron spectroscopy mapping. Micro-heterogeneities characteristics for all samples are summarized in table 2.

### 3.2. Macrorheological characterization: slip, shear-induced fracture and elasticity

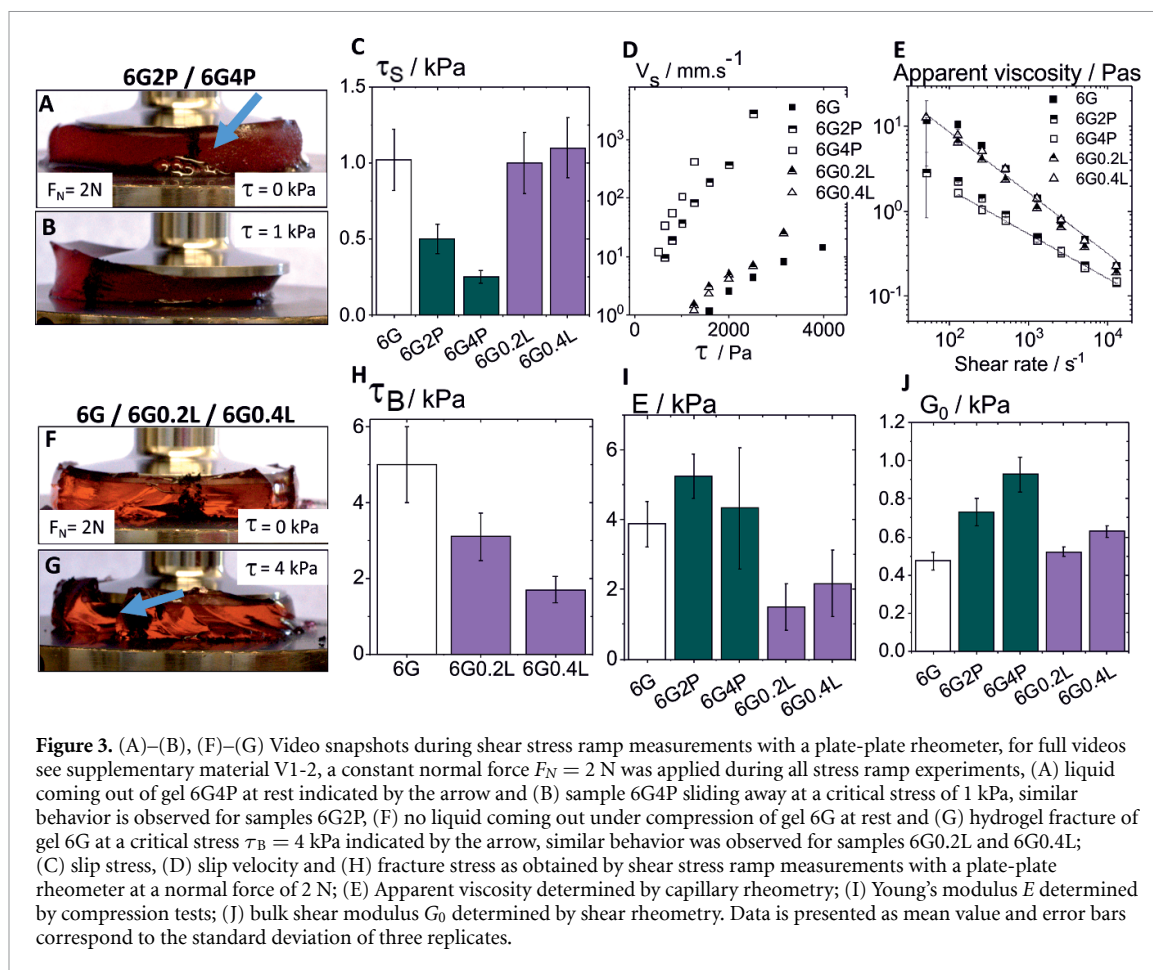
PVA demixing from gelatin matrix leads to formation of a liquid phase that can potentially act as a lubrication layer for the hydrogel during extrusion. Based on this hypothesis, experiments were performed with the rotational rheometer in order to evaluate the slip behavior of the samples. The onset of slip is characterized by the critical shear stress  $\tau_s$  necessary for the upper plate to rotate while the hydrogel remains intact. The video snapshots reveal that polymer solution is released from the gels when compressing samples including PVA (see figure 3(A)). This liquid phase is also responsible for the sample to slide away from parallel plate geometry at high shear stresses even before it breaks (figure 3(B)). Figure 3(A) shows a snapshot right after the sample 6G4P was compressed ( $F_N = 2$  N) by the plate geometry before the measurement started (shear stress  $\tau = 0$  Pa). When compressed, PVA solution from the micro-pores is expelled, as pointed by the arrow. Figure 3(B) shows the pronounced wall slip behavior of sample 6G4P during rotational rheometry measurement. At shear

stresses higher than  $\tau_s$ , the sample begins to slip and eventually slides away from the plate geometry. The snapshot was taken at shear stress  $\tau = 1$  kPa. For better visualization of the wall slip effect on the gel 6G4P, the video V1 is available in the supplementary material.

This pronounced slip behavior is not observed for the pure gelatin gel and the gelatin/Laponite composites (6G, 6G0.2L and 6G0.4L), in which no liquid spillage takes place during compression (figure 3(F)). The lack of lubrication leads to eventual gel fracture at high shear stresses (figure 3(G)). Video recordings of these experiments are found in the supplementary material (V1 and V2).

The critical slip stress values for gels 6G, 6G0.2L and 6G0.4L were very similar,  $\tau_s \approx 1000$  Pa (figure 3(C)). Gels with PVA, on the other hand, start slipping at much lower shear stresses due to lubrication layer ( $\tau_s \approx 500$  Pa for sample 6G2P and  $\tau_s \approx 250$  Pa for sample 6G4P). For shear stresses higher than the slip stress, the apparent slip velocity was determined at the rim of the rotating plate (equation (1)). Again, pronounced slip behavior is observed for samples with PVA as the slip velocity for these gels is approximately 2 orders of magnitude higher than for pure gelatin and mixed gelatin/Laponite gels when compared at a given shear stress (figure 3(D)). This slip phenomenon for samples 6G2P and 6G4P is expected to play a crucial role during EBB as well. This shows up directly in the flow curves obtained from capillary rheometry. In this technique samples are extruded through a capillary using a piston, mimicking the EBB process. Apparent viscosity curves for gelatin and mixed gelatin/Laponite gels (samples 6G, 6G0.2L and 6G0.4L) shown in figure 3(E) are very similar, showing that Laponite aggregates do not affect gel apparent flow behavior. For samples with PVA, however, a drop in viscosity is observed in the whole shear rate range investigated, which is associated with the pronounced slip behavior.

The brittle behavior observed in pure gelatin gels is even more pronounced when Laponite is introduced. Samples 6G0.2L and 6G0.4L break at lower shear stress  $\tau_B \leq 3$  kPa in comparison to sample 6G,  $\tau_B \approx 5$  kPa (figure 3(H)). Uniaxial compression tests also show a pronounced drop in the Young's modulus  $E$  for gels with Laponite in comparison to pure gelatin and samples with PVA (figure 3(I)). This is presumably due to the polymer/nanoclay agglomerates acting as stress concentration spots in the hydrogel. These highly stressed regions can lead to localized yielding and plastic deformation of the material [44]. Load-bearing particulate aggregates undergo non-affine deformation that induces buckling and accelerates material failure [45]. The brittle characteristic of mixed gelatin/Laponite gels under compression is expected to affect its performance in EBB as well.



Gelatin is usually functionalized, allowing for a chemical crosslinking to a stable scaffold for tissue engineering. The functionalization and the rate of crosslinks within the gelatin hydrogels influences the pore size and the mechanical properties. Tuning of crosslinking density and mechanical properties is of great relevance for growth and differentiation of living cells in gelatin hydrogels [46]. An increase in shear elastic modulus  $G_0$  was observed for both strategies of micro-heterogeneity formation presented in this study, despite the absence of gelatin functionalization (figure 3(J)). Even though PVA is not crosslinked and remains in solution, hence not directly contributing to the elasticity,  $G_0$  increases from 475 Pa (sample 6G) to 927 Pa (sample 6G4P). For comparison, a gelatin concentration, i.e. amount of physically cross-linked polymer, of 8 wt.% is required to obtain a modulus  $G_0 = 1000\text{ Pa}$  in a uniform gel (figure S4). A densely crosslinked polymer network can impair nutrient diffusion and cell proliferation [8], aside from enhancing cell damage while printing due to higher viscosity and thus higher shear stresses [47]. The addition of PVA increases elasticity in a comparable way without further addition of crosslinked polymer and at the same time induces a porous configuration. Similarly, an investigation conducted with alginate based hydrogels shows that a gel with lower alginate content but enhanced heterogeneity exhibits

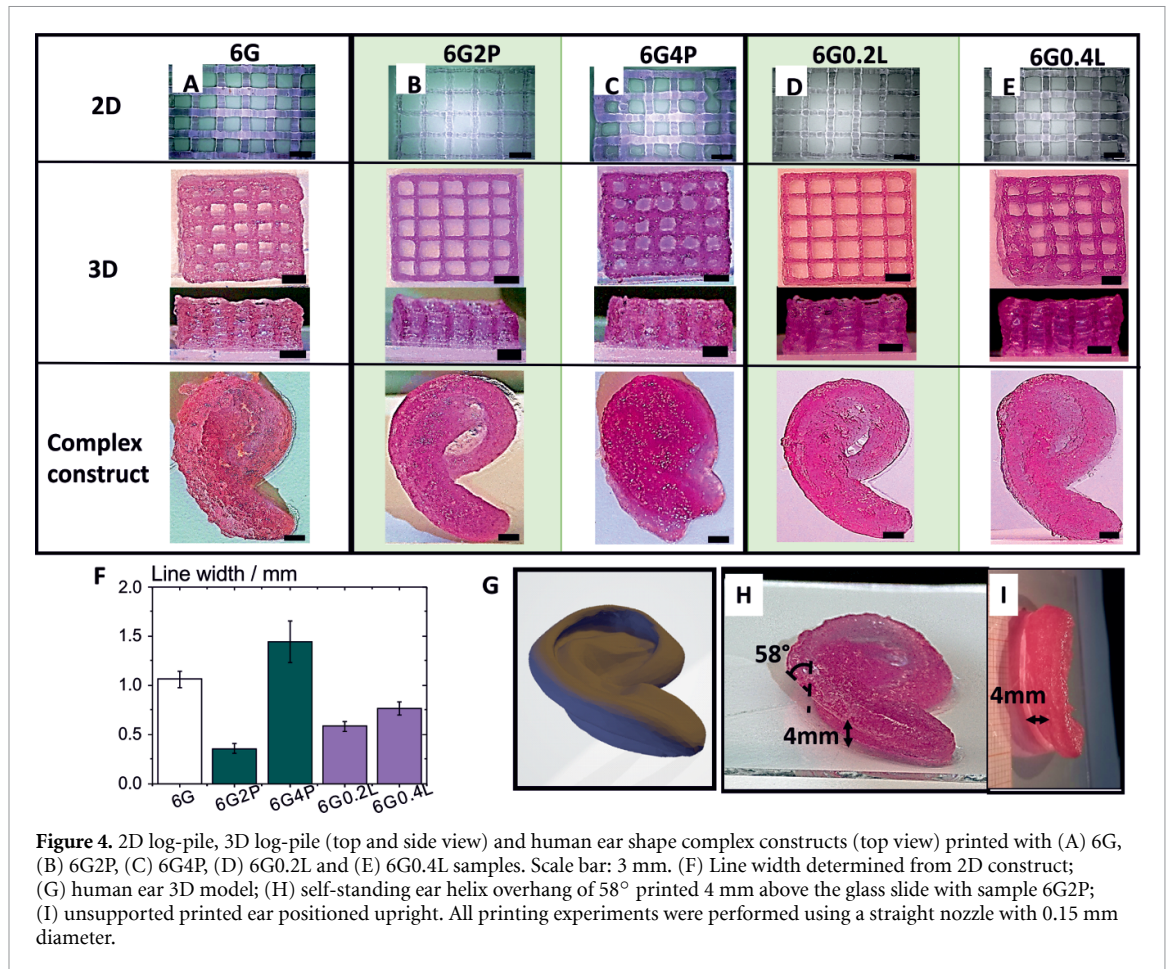
elasticity equivalent to a more homogeneous gel with higher polymer content (figure S5).

In addition, the gelatin/Laponite interaction and aggregate formation leads to an increase in  $G_0$  from 475 Pa (sample 6G) to 630 Pa (sample 6G0.4L). This elasticity enhancement at small shear deformations due to micro-heterogeneities generated in gelatin gels is expected to show positive effects on the mechanical stability of 3D printed constructs.

### 3.3. EBB: printing quality evaluation

The printing quality of the hydrogels was evaluated in three steps: 2D log pile geometry (two printed layers), 3D log pile (5 mm high and 15 mm length) and complex construct (human ear shape, 7 mm high and 3 cm length), without supporting material.

All gels show high shape fidelity regarding the log pile geometry (line width  $< 1.5\text{ mm}$ ) when 2D constructs are printed (figures 4(A)–(E)). Hydrogels including only a small fraction of viscous droplets or dense particle clusters (6G2P and 6G0.2L, see table 2), however, display distinctly improved line quality, with thinner (line width  $< 0.6\text{ mm}$ , figure 4(F)) and more uniform lines than pure gelatin (6G, line width  $\sim 1\text{ mm}$ ) and gels with more pronounced heterogeneity (6G4P and 6G0.4L, line width  $> 0.75\text{ mm}$ ). Note, the higher shear modulus of the heterogeneous hydrogels does not necessarily lead to a decrease

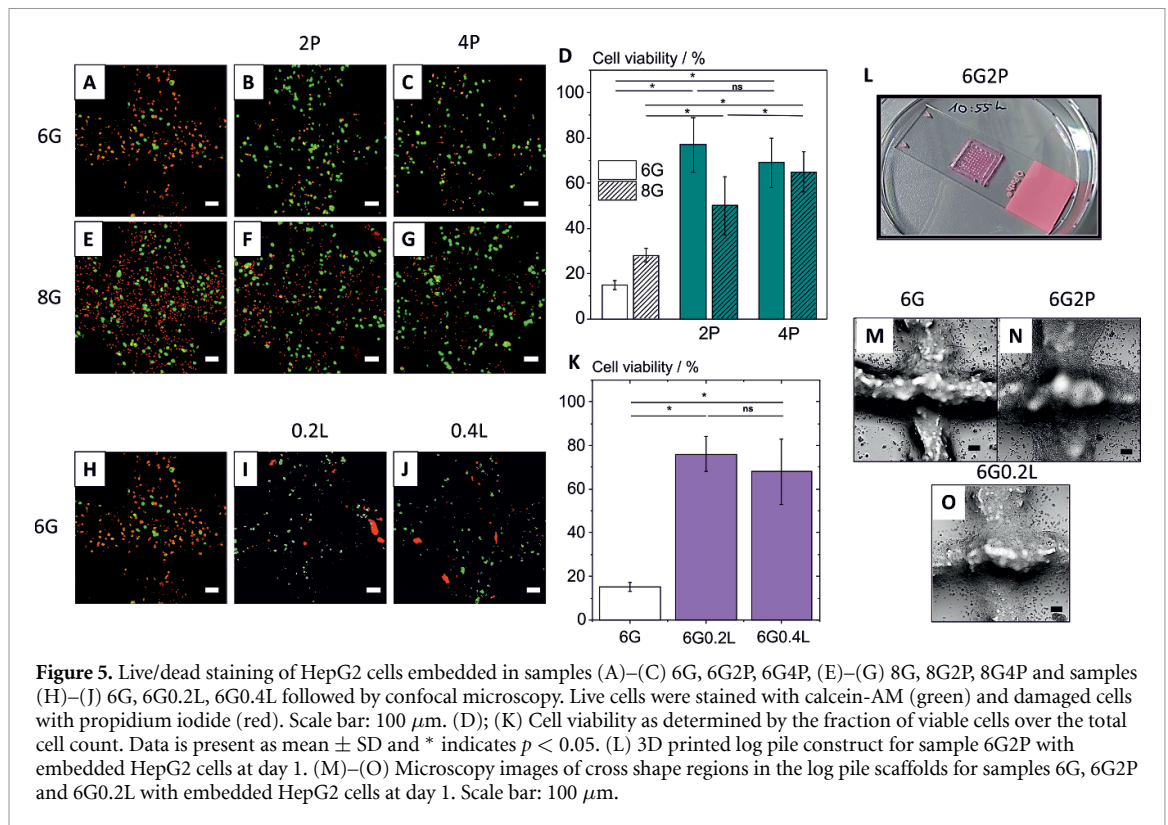


in line width, which is observed for homogeneous pure gelatin gels (figure S4). This suggests that the slip or gel fracture phenomena described above may also contribute to the print quality of such gels, likewise the proportion and magnitude of heterogeneities could play a role in the uniformity of the printed lines.

When more layers are added and 3D constructs are printed, the disparity in printing quality becomes more relevant. Finer printed lines obtained from gels 6G2P and 6G0.2L form 3D constructs with superior top surface geometrical accuracy. This superior printability with moderately heterogeneous gels appears to be essential for complex constructs 3D printing, as good resolution and excellent shape fidelity were achieved with gels 6G2P and 6G0.2L when printing a human ear geometry. The human ear 3D model is a complex object with a rounded shape which displays more details than the simpler grid geometry (figure 4(G)). Self-standing ear helix overhangs of approximately 58° were successfully printed 4 mm above the glass slide with sample 6G2P (figure 4(H)). Moreover, all the printed constructs display mechanical stability provided by the high elastic shear modulus, and they do not collapse when positioned upright (see figure 4(I) for sample 6G2P). The pure gelatin gel 6G and also the mixed gels with pronounced heterogeneity 6G4P and 6G0.4L did not provide good

resolution for complex shaped constructs and failed in terms of shape fidelity.

The presence of viscous pore-like inclusions in 6G2P gel enhances slip behavior while polymer-nanoclay aggregates in 6G0.2L gel promote brittle failure and lead to gel fracture at lower stresses than pure gelatin. Regardless of whether the micro-heterogeneities are viscous or solid, both of these phenomena facilitate extrusion, allowing the fabrication of complex 3D constructs with excellent printing quality. However, this is not observed for samples 6G4P and 6G0.4L, in which the micro-heterogeneities are larger and their fraction is higher (>20%). While targeted introduction of micro-phase separation is shown to significantly improve extrusion in comparison to the homogeneous gel, the size and amount of the micro-heterogeneities has to be limited for successful high quality printing. For uniform filament extrusion, the micro-heterogeneity dimensions should be considerably smaller than the printed feature size, namely the nozzle diameter. As a rule of thumb, particle aggregates should be ten times smaller than the nozzle size to avoid clogging [48] or filament interruptions in case of freely flowing viscous inclusions. For the systems studied here, a 150  $\mu\text{m}$  diameter nozzle was employed and positive results were obtained for gels with small inclusion



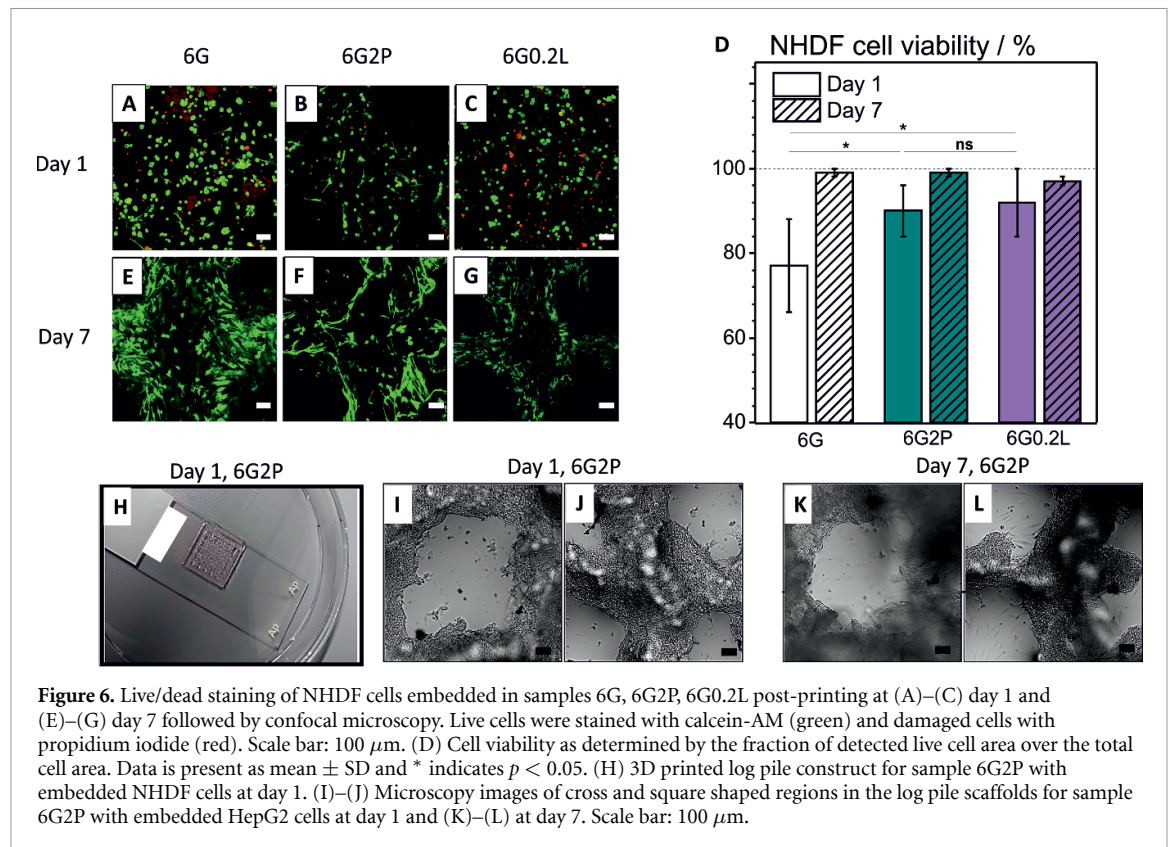
size ( $5 \pm 2 \mu\text{m}$  for sample 6G2P) as well as with larger micro-heterogeneities ( $34 \pm 14 \mu\text{m}$  for sample 6G0.2L) that, however, are scarcely present ( $4 \pm 3\%$  of the total hydrogel area). On the other hand, larger viscous inclusions or aggregates ( $>28 \mu\text{m}$ ) amounting to more than 24% of hydrogel fraction (samples 6G4P and 6G0.4L) impair filament uniformity. Similarly, for alginate based hydrogels, several small viscous inclusions (up to  $12 \pm 6 \mu\text{m}$ ) which amount to 18% of the hydrogel volume allow for uniform filament printing in 2D (figure S5), while few large micro-heterogeneities that reach  $100 \mu\text{m}$  in size disrupt filament uniformity.

### 3.4. 3D bioprinting: cell viability

Bioprinting experiments were performed with human hepatocarcinoma HepG2 cells embedded in the 6 wt.% and 8 wt.% gelatin based hydrogels to evaluate the impact of the 3D printing process on the cell viability. Details on bulk and micro-mechanical properties of the samples with 8 wt.% gelatin can be found in the supplementary material (figure S6). Log pile structures of four layers were printed at  $20^\circ\text{C}$ . The minimum amount of mTG necessary for stably crosslinking the hydrogels for the respective cell culture time was used. Namely, 10% mTG was used for day 1 and 20% mTG for 7 d of cell culture. Live/dead assay (figures 5(A)–(G)) reveals high cell viability at day 1 for hydrogels with PVA ( $>50\%$  for 8% and  $>65\%$  for 6% gelatin compositions) (figure 5(D)), while viability was considerably lower for homogeneous pure gelatin hydrogels ( $<35\%$  for both 6G and

8G samples). The slip induced by the viscous PVA inclusions leads to a dominating plug flow and the contribution of shear deformation to gel transport during extrusion is low. This presumably protects the cells, causing less damage and improving viability. The viability for HepG2 cells at day 7 was tested for samples 6G and 6G4P and live/dead staining images can be found in figure S7. The higher cell viability obtained for hydrogels with PVA in comparison to pure gelatin at day 1 seems to be qualitatively maintained at day 7 of cell culture (figure S7).

Similarly, printing with hydrogel composites including Laponite (6G0.2L and 6G0.4L) resulted in higher cell viability  $>65\%$  (figures 5(H)–(K)). This suggests, that the brittle behavior caused by the nanoclay aggregates, which facilitates extrusion also mitigates cell damage during printing and actually increases cell viability. A brittle fracture takes place with little or no plastic deformation and low energy absorption [44]. Therefore, the cells embedded in the gelatin hydrogels with Laponite nanoclay experienced a lower deformation in comparison to cells embedded in pure gelatin samples. The brittle behavior of gelatin/Laponite gels results in a lower capacity of transferring deformation related shear stress to the living cells while printing, hence increasing cell viability. Cell viability values after printing were normalized with the non-printed control. It is worth noting that Laponite agglomerates present in 0.2L and 0.4L gels interact with propidium iodide used to stain non-viable cells, corresponding to the non-cell like red shapes in the images. The presence



of these large agglomerates was excluded from the evaluation by normalizing the cell viability with the controls.

A log pile structure of four layers printed on adhesive glass slide is shown exemplarily for sample 6G2P with embedded HepG2 cells at day 1 in figure 5(l). Details on the regions where printed filaments cross can be seen in figures 5(M)–(O) for samples 6G, 6G2P and 6G0.2L.

Normal human dermal fibroblasts NHDF cells were embedded in the homogeneous sample 6G and in the weakly heterogeneous samples 6G2P and 6G0.2L, which provided excellent printability and higher viability with HepG2 cells. Hydrogels were printed in log pile geometries of four layers and cell viability was analyzed on day 1 to evaluate direct 3D printing impact (figures 6(A)–(C)) and on day 7 of cell culture (figures 6(E)–(G)). On day 1, hydrogel 6G showed cell viability <80%, while gels 6G2P and 6G0.2L presented an improved viability >85% (figure 6(D)). On day 7, cells exhibited elongation with similar morphology in all gels. NHDF cells were more concentrated on the rim of the hydrogel and viability was >90% for all samples.

A log pile scaffold of four layers printed on adhesive glass slide is shown exemplarily for sample 6G2P with embedded NHDF cells at day 1 in figure 6(H). Details on the regions where printed filaments cross as well as on the void regions between filaments can be seen in figures 6(I) and (J) for samples 6G2P at day 1 and in figures 6(K) and (L) at day 7.

Extensive research over the last decades has established that gelatin-based gels provide good environment for cell proliferation [49, 50]. However, much less is known about mechanisms of micro-heterogeneity formation and how to control it in such gels. In this study, we developed two different gelatin-based bioinks with tailored micro-heterogeneity which allow for fabrication of complex 3D constructs with excellent printability and provide cell viability significantly higher than in uniform gelatin gels right after printing as well as after 7d of cell culture.

#### 4. Discussion

Targeted micro-phase separation generates highly elastic bioinks with a complex micro-structure. Here we investigated non-functionalized gelatin-based gels and characterized the introduced microheterogeneities with respect to their size, shape, volume fraction, and local mechanical properties using MPT microrheology. Generally, micro-heterogeneity formation in hydrogels leads to an increase in the bulk shear modulus, but other effects on bulk mechanical behavior were observed depending on the heterogeneity type. Gelatin/PVA hydrogels with their viscous PVA inclusions presented distinct slip behavior with a low critical stress  $\tau_s$  at which slip sets in and a very high slip velocity at stresses  $\tau > \tau_s$ . Gelatin/Laponite composites include dense nanoclay/polymer clusters resulting in brittle behavior under compression and a

reduced shear stress  $\tau_B$  at which the hydrogels break. Although the effects of both types of heterogeneities on the macro-mechanical properties are evidently different, in both cases smooth material extrusion at 20 °C and reduced damage to cells during EBB is observed. Objects with excellent resolution, i.e., higher precision due to uniform thin filaments (width < 0.6 mm), could be obtained without support material by using moderately heterogeneous composite gels. However, size and fraction of heterogeneous inclusions has to be adjusted carefully in order to obtain excellent printing quality. The length scale of the heterogeneities must be well below the nozzle outlet diameter and the fraction of the (soft and viscous or solid) inclusions should not be too high (<24%) in order to achieve interruption free, uniform filaments. In this study we developed heterogeneous, highly elastic gels that allow for printing of complex self-standing 3D structures at room temperature with better resolution, shape retention and higher cell viability in comparison to the equivalent homogeneous gelatin hydrogel. Cell viability directly after printing was drastically increased when printing human hepatocarcinoma HepG2 cells embedded in heterogeneous gels. The effect was less pronounced for normal human dermal fibroblasts NHDF cells which exhibit a fairly high viability even if embedded in a homogeneous gelatin bioink. Current bioprinting strategies often adopt larger (diameter > 0.41 mm), conical nozzles in order to increase cell viability. Besides, gelatin-based hydrogels are commonly printed at higher temperatures (>25 °C) in order to obtain a liquid or smooth material that is less capable of transferring shear stresses to the living cells. Our study shows that moderately heterogeneous gelatin-based hydrogels provide a much higher cell viability in comparison to the equivalent homogeneous hydrogel even when smaller (0.25 mm outlet diameter), cylindrical nozzles are employed and temperature is kept at 20 °C (solid state gelatin). It is worth mentioning that, in this study, bioprinting was conducted using only cylindrical needles and high cell viability soon after printing (>65% with 6% gelatin gels) was achieved due to the bioink design developed here. However, other printing parameters can be adjusted with the aim of improving cell viability, such as printing pressure and nozzle type. Employing conical nozzles might allow the cell viability to achieve even higher levels due to reduced cell exposure to shear forces [51].

Moreover, further research should be conducted on functional analysis after printing and over time of specific cell lines and its correlation with the micro-heterogeneities formation in the bioink. Cell specific physiological processes, such as motility as well as gene and protein expression, should be tested in order to gain insight on the effect of micro-heterogeneities on the cell lines function.

## 5. Conclusion

In this study, hydrogels which presented balanced heterogeneity allowed 3D printing of self-standing complex constructs at room temperature without a support material and provided high NHDF cell viability after 7 d of cell culture. MPT microstructural characterization can help tailor favorable microenvironment conditions and bulk elasticity for 3D printing with living cells. Modulation of the microstructure via inducing viscous pore-like inclusions or micro-heterogeneity formation caused by polymer-nanoclay interactions in gelatin networks is of great importance for printing quality as well as supportive microenvironment development for cell 3D printing. The concept of introducing micro-heterogeneities can be transferred to other hydrogel systems in a straight forward manner and thus may stimulate development of further strategies for improving print quality and cell viability.

## Data availability statements

All data that support the findings of this study are included within the article (and any supplementary files).

## Acknowledgments

The authors would like to thank Julian Petermann for performing measurements on the rotational and capillary rheometer. Research was funded by the Deutsche Forschungsgemeinschaft (DFG, German Research Foundation) under Germany's Excellence Strategy via the Excellence Cluster 3D Matter Made to Order (EXC-2082/1–390761711). The research was also supported by the Helmholtz Program Information: Materials Systems Engineering.

## Conflict of interest

The authors declare no conflicts of interest.

## ORCID iD

Bruna R Maciel  <https://orcid.org/0000-0001-7837-2582>

## References

- [1] Ng W L, Chua C K and Shen Y-F 2019 Print me an organ! Why we are not there yet *Prog. Polym. Sci.* **97** 101145
- [2] Kumar A and Han S S 2017 PVA-based hydrogels for tissue engineering: a review *Int. J. Polym. Mater. Polym. Biomater.* **66** 159–82
- [3] Li J, Wu C, Chu P K and Gelinsky M 2020 3D printing of hydrogels: Rational design strategies and emerging biomedical applications *Mater. Sci. Eng. R* **140** 100543
- [4] Vega S L, Kwon M Y and Burdick J A 2017 Recent advances in hydrogels for cartilage tissue engineering *Eur. Cell Mater.* **33** 59–75

- [5] Hago E and Li X 2013 Interpenetrating polymer network hydrogels based on gelatin and PVA by biocompatible approaches: synthesis and characterization *Adv. Mater. Sci. Eng.* **2013** 328763
- [6] Kim H, Yang G H, Choi C H, Cho Y S and Kim G 2018 Gelatin/PVA scaffolds fabricated using a 3D-printing process employed with a low-temperature plate for hard tissue regeneration: fabrication and characterizations *Int. J. Biol. Macromol.* **120** 119–27
- [7] Miao T, Miller E J, McKenzie C and Oldinski R A 2015 Physically crosslinked polyvinyl alcohol and gelatin interpenetrating polymer network theta-gels for cartilage regeneration *J. Mater. Chem. B* **3** 9242–9
- [8] Chimene D, Kaunas R and Gaharwar A K 2020 Hydrogel bioink reinforcement for additive manufacturing: a focused review of emerging strategies *Adv. Mater.* **32** e1902026
- [9] Jiang Y, Krishnan N, Heo J, Fang R H and Zhang L 2020 Nanoparticle–hydrogel superstructures for biomedical applications *J. Control. Release* **324** 505–21
- [10] Afewerki S, Magalhães L S S M, Silva A D R, Stocco T D, Filho E C S, Marciano F R and Lobo A O 2019 Bioprinting a synthetic smectic clay for orthopedic applications *Adv. Healthcare Mater.* **8** 1900158
- [11] Ahlfeld T, Cidonio G, Kilian D, Duin S, Akkineni A R, Dawson J I, Yang S, Lode A, Oreffo R O C and Gelinsky M 2017 Development of a clay based bioink for 3D cell printing for skeletal application *Biofabrication* **9** 34103
- [12] Cai F-F, Heid S and Boccaccini A R 2021 Potential of Laponite® incorporated oxidized alginate–gelatin ( ADA-GEL ) composite hydrogels for extrusion-based 3D printing *J. Biomed. Mater. Res. B* **109** 1090–104
- [13] Heid S and Boccaccini A R 2020 Advancing bioinks for 3D bioprinting using reactive fillers: a review *Acta Biomater.* **113** 1–22
- [14] Malekpour A and Chen X 2022 Printability and cell viability in extrusion-based bioprinting from experimental, computational, and machine learning views *J. Funct. Biomater.* **13** 40
- [15] Mao H, Yang L, Zhu H, Wu L, Ji P, Yang J and Gu Z 2020 Recent advances and challenges in materials for 3D bioprinting *Prog. Nat. Sci.* **30** 618–34
- [16] Lee A, Hudson A R, Shiwarski D J, Tashman J W, Hinton T J, Yerneni S, Bliley J M, Campbell P G and Feinberg A W 2019 3D bioprinting of collagen to rebuild components of the human heart *Science* **365** 482–7
- [17] Chimene D, Peak C W, Gentry J L, Carrow J K, Cross L M, Mondragon E, Cardoso G B, Kaunas R and Gaharwar A K 2018 Nanoengineered ionic–covalent entanglement (NICE) bioinks for 3D bioprinting *ACS Appl. Mater. Interfaces* **10** 9957–68
- [18] Ashammakhi N, Ahadian S, Xu C, Montazerian H, Ko H, Nasiri R, Barros N and Khademhosseini A 2019 Bioinks and bioprinting technologies to make heterogeneous and biomimetic tissue constructs *Mater. Today Bio.* **1** 100008
- [19] Cidonio G, Glinka M, Dawson J I and Oreffo R O C 2019 The cell in the ink: improving biofabrication by printing stem cells for skeletal regenerative medicine *Biomaterials* **209** 10–24
- [20] Lalitha Sridhar S, Schneider M C, Chu S, Roucy G D, Bryant S J and Vernerey F J 2017 Heterogeneity is key to hydrogel-based cartilage tissue regeneration *Soft Matter* **13** 4841–55
- [21] Hafner J, Oelschlaeger C and Willenbacher N 2020 Microrheology imaging of fiber suspensions—a case study for lyophilized collagen I in HCl solutions *Soft Matter* **16** 9014–27
- [22] Soto A M, Koivisto J T, Parraga J E, Silva-Correia J, Oliveira J M, Reis R L, Kellomäki M, Hyttinen J and Figueiras E 2016 Optical projection tomography technique for image texture and mass transport studies in hydrogels based on gellan gum *Langmuir* **32** 5173–82
- [23] Vielreicher M, Schürmann S, Detsch R, Schmidt M A, Buttgerit A, Boccaccini A and Friedrich O 2013 Taking a deep look: modern microscopy technologies to optimize the design and functionality of biocompatible scaffolds for tissue engineering in regenerative medicine *J. R. Soc. Interface* **10** 20130263
- [24] Moschakis T 2013 Microrheology and particle tracking in food gels and emulsions *Curr. Opin. Colloid Interface Sci.* **18** 311–23
- [25] Hafner J *et al* 2020 Monitoring matrix remodeling in the cellular microenvironment using microrheology for complex cellular systems *Acta Biomater.* **111** 254–66
- [26] McKenna M, Shackelford D, Ferreira Pontes H, Ball B and Nance E 2021 Multiple particle tracking detects changes in brain extracellular matrix and predicts neurodevelopmental age *ACS Nano* **15** 8559–73
- [27] Roether J, Bertels S, Oelschlaeger C, Bastmeyer M and Willenbacher N 2018 Microstructure, local viscoelasticity and cell culture suitability of 3D hybrid HA/collagen scaffolds *PLoS One* **13** e0207397
- [28] Maciel B R, Wang K, Müller M, Oelschlaeger C and Willenbacher N 2023 Targeted micro-phase separation—A generic design concept to control the elasticity of extrudable hydrogels *Mater. Des.* **227** 111803
- [29] Dai W, Zhang L, Yu Y, Yan W, Zhao F, Fan Y, Cao C, Cai Q, Hu X and Ao Y 2022 3D bioprinting of heterogeneous constructs providing tissue-specific microenvironment based on host–guest modulated dynamic hydrogel bioink for osteochondral regeneration *Adv. Funct. Mater.* **32** 2200710
- [30] Xu H-Q, Liu J-C, Zhang Z-Y and Xu C-X 2022 A review on cell damage, viability, and functionality during 3D bioprinting *Mil. Med. Res.* **9** 70
- [31] Fischer L *et al* 2022 Calcium supplementation of bioinks reduces shear stress-induced cell damage during bioprinting *Biofabrication* **14** 045005
- [32] Emmermacher J, Spura D, Cziommer J, Kilian D, Wollborn T, Fritsching U, Steingroewer J, Walther T, Gelinsky M and Lode A 2020 Engineering considerations on extrusion-based bioprinting: interactions of material behavior, mechanical forces and cells in the printing needle *Biofabrication* **12** 25022
- [33] Kowalczyk A, Oelschlaeger C and Willenbacher N 2015 Visualization of micro-scale inhomogeneities in acrylic thickener solutions: a multiple particle tracking study *Polymer* **58** 170–9
- [34] Bubeck R, Bechinger C, Naser S and Leiderer P 1999 Melting and reentrant freezing of two-dimensional colloidal crystals in confined geometry *Phys. Rev. Lett.* **82** 3364–7
- [35] Naser S, Bechinger C, Leiderer P and Palberg T 1997 Finite-size effects on the closest packing of hard spheres *Phys. Rev. Lett.* **79** 2348–51
- [36] Crocker J C and Grier D G 1995 Methods of digital video microscopy for colloidal studies *J. Colloid Interface Sci.* **179** 298–310
- [37] Mason T G 2000 Estimating the viscoelastic moduli of complex fluids using the generalized Stokes-Einstein equation *Rheol. Acta* **39** 371–8
- [38] Wirtz D 2009 Particle-tracking microrheology of living cells: principles and applications *Annu. Rev. Biophys.* **38** 301–26
- [39] Mason T G and Weitz D A 1995 Optical measurements of frequency-dependent linear viscoelastic moduli of complex fluids *Phys. Rev. Lett.* **74** 1250–3
- [40] Alberti S, Gladfelter A and Mittag T 2019 Considerations and challenges in studying liquid-liquid phase separation and biomolecular condensates *Cell* **176** 419–34
- [41] Fernández-Rico C, Sai T, Sicher A, Style R W and Dufresne E R 2022 Putting the squeeze on phase separation *J. Am. Chem. Soc.* **2** 66–73
- [42] Pawar N and Bohidar H B 2009 Surface selective binding of nanoclay particles to polyampholyte protein chains *J. Chem. Phys.* **131** 45103
- [43] Sheikhi A, Afewerki S, Oklu R, Gaharwar A K and Khademhosseini A 2018 Effect of ionic strength on

- shear-thinning nanoclay–polymer composite hydrogels *Biomater. Sci.* **6** 2073–83
- [44] Callister W D JR. 2001 *Fundamentals of Materials Science and Engineering* 5th edn (Wiley)
- [45] Islam M M and Lester D R 2021 Superposed shear and compression of strong colloidal gels *J. Rheol.* **65** 837–53
- [46] Sung B, Krieger J, Yu B and Kim M-H 2018 Colloidal gelatin microgels with tunable elasticity support the viability and differentiation of mesenchymal stem cells under pro-inflammatory conditions *J. Biomed. Mater. Res. A* **106** 2753–61
- [47] Hull S M, Brunel L G and Heilshorn S C 2022 3D bioprinting of cell-laden hydrogels for improved biological functionality *Adv. Mater.* **34** e2103691
- [48] Marnot A, Dobbs A and Brettmann B 2022 Material extrusion additive manufacturing of dense pastes consisting of macroscopic particles *MRS Commun.* **12** 483–94
- [49] Bello A B, Kim D, Kim D, Park H and Lee S-H 2020 Engineering and functionalization of gelatin biomaterials: from cell culture to medical applications *Tissue Eng. B* **26** 164–80
- [50] Djagny K B, Wang Z and Xu S 2001 Gelatin: a valuable protein for food and pharmaceutical industries: review *Crit. Rev. Food Sci. Nutr.* **41** 481–92
- [51] Adhikari J, Roy A, Das A, Ghosh M, Thomas S, Sinha A, Kim J and Saha P 2021 Effects of processing parameters of 3D bioprinting on the cellular activity of bioinks *Macromol. Biosci.* **21** e2000179